

On-the-fly *ab initio* semiclassical dynamics: Identifying degrees of freedom essential for emission spectra of oligothiophenes

Marius Wehrle, Miroslav Šulc, and Jiří Vaníček^{a)}

Laboratory of Theoretical Physical Chemistry, Institut des Sciences et Ingénierie Chimiques, Ecole Polytechnique Fédérale de Lausanne (EPFL), CH-1015, Lausanne, Switzerland

(Dated: May 28, 2022)

Vibrationally resolved spectra provide a stringent test of the accuracy of theoretical calculations. We combine the thawed Gaussian approximation (TGA) with an on-the-fly *ab initio* (OTF-AI) scheme to calculate the vibrationally resolved emission spectra of oligothiophenes with up to five rings. The efficiency of the OTF-AI-TGA permits treating all vibrational degrees of freedom on an equal footing even in pentathiophene with 105 vibrational degrees of freedom, thus obviating the need for the global harmonic approximation, popular for large systems. Besides reproducing almost perfectly the experimental emission spectra, in order to provide a deeper insight into the associated physical and chemical processes, we also develop a novel systematic approach to assess the importance and coupling between individual vibrational degrees of freedom during the dynamics. This allows us to explain how the vibrational line shapes of the oligothiophenes change with increasing number of rings. Furthermore, we observe the dynamical interplay between the quinoid and aromatic characters of individual rings in the oligothiophene chain during the dynamics and confirm that the quinoid character prevails in the center of the chain.

^{a)}Electronic mail: jiri.vanicek@epfl.ch

I. INTRODUCTION

Polythiophenes (T_n) and their functional derivatives belong among the most studied compounds among π -conjugated polymers due to their potential in organic electronics,¹ since they combine remarkable conductivity with excellent thermo- and chemo-stability. Detailed experimental investigations of polythiophenes have shown that their optical properties are closely related to the structure of the polymer backbone: For instance, the 0–0 transition energies are approximately a linear function of $1/n$, where n is the number of thiophene rings in the polymer.^{2–4} Bandgap computations confirmed validity of this semi-empirical rule for short polymers as well as its violation for longer chains.^{5,6}

For a direct comparison with experiments it is, however, crucial to calculate the vibrationally resolved spectra.^{7,8} Here, we therefore determine the vibrationally resolved emission spectra of oligothiophenes T_n with two to five rings, i.e., $n \in \{2, 3, 4, 5\}$, since the vibrational line shape is changing drastically in this range of n .²

The cost of computing a vibrationally resolved spectrum is much higher than the cost of vertical transition energy calculations since the spectrum calculation requires the knowledge of the involved potential energy surfaces (PESs). As it is often difficult to describe PESs accurately in terms of analytical functions, a popular approach, especially for larger molecules is to approximate the PESs by harmonic potentials with respect to certain reference structures.^{9,10} The absorption and emission line shapes of dithiophene have been calculated by Stendardo *et al.*¹¹ using a double-well potential describing the torsional mode and global harmonic approximation in the remaining degrees of freedom. In order to get a good correspondence with experiment, the authors show that an appropriate choice of these reference structures is essential, e.g., the ground PES reference structure for the emission spectrum calculation is found using symmetry constraints.

Alternative strategy employs trajectory-based methods in combination with an on-the-fly (OTF) *ab initio* (AI) scheme, in which the required potential energies, forces, and Hessians are computed with an electronic structure package during the dynamics. It is becoming increasingly clear that *ab initio* semiclassical dynamics provides a powerful spectroscopic tool useful, e.g., for evaluating internal conversion rates¹² or vibrationally resolved spectra.^{13–15} Not only do the evolving trajectories provide an intuitive classical-like picture of the underlying physical and chemical processes, but via interference, they also partially account

for the most important nuclear quantum effects. The overall computational cost, however, restricts almost all of these methods to small systems.

As a result, one is forced to strike a balance between physical accuracy and computational efficiency. In this spirit, OTF-AI Gaussian wave packet propagation can provide a useful compromise. Within the thawed Gaussian approximation (TGA), the nuclear wave packet is guided by a central classical trajectory, which feels the anharmonicity of the potential, while its width is propagated using the local harmonic approximation.¹⁶ Hence, the effects of anharmonic or double-well potentials are partially captured by TGA; moreover, the OTF-AI framework obviates the need of an a priori knowledge of the landscape of the final PES. More importantly, due to its moderate computational cost, TGA can treat all vibrational degrees of freedom on an equal footing even in large systems, while in smaller systems, it permits using a more accurate electronic structure description. A well-known shortcoming of the TGA is that it captures accurately only the short-time dynamics and, therefore, only describes the broad spectral features.¹⁷ Nevertheless, due to interaction with solvent and other phenomena contributing to spectral broadening, the experimental spectra are also typically not fully vibrationally resolved.

Although rewarding, a mere reproduction of an experimental spectrum, no matter how accurate, does not provide a deeper insight into the associated physical and chemical processes; it is a careful analysis of the simulation that can provide such information. The extraction of this essential information, which is often omitted, can be as difficult as the simulation itself, especially for larger molecules. For example, explanation of changes in the vibrational line shape of the spectra due to increasing polymer chain length, which is done here for oligothiophenes, increases drastically the complexity of the analysis. Therefore, in addition to providing an efficient computational protocol for computing vibrationally resolved electronic spectra we also present a systematic approach for extracting the essential information about the underlying dynamics.

II. THEORY

A. Emission spectrum calculation

In the time-dependent approach pioneered by Heller,¹⁷ the molecular spectrum is determined by the Fourier transform of an appropriate correlation function. Within the electric dipole approximation, time-dependent perturbation theory, and rotating wave approximation, the correlation function required for computing the emission spectrum is

$$C_{\text{em}}(t) \propto \text{Tr} \left[\hat{\rho}_1(T) \hat{\mu}_{10} \hat{U}_0(-t) \hat{\mu}_{01} \hat{U}_1(t) \right]. \quad (1)$$

Here, $\hat{\rho}_1(T)$ is the nuclear density operator in the first excited electronic state (S_1) at temperature T , $\hat{U}_j(t) = \exp(-i\hat{H}_j t/\hbar)$ for $j \in \{0, 1\}$ denotes the nuclear quantum evolution operator on the j th electronic surface S_j , and $\hat{\mu}_{ij}$ is the transition dipole moment operator coupling states S_i and S_j . Within the Franck-Condon approximation and in the low temperature limit, the correlation function (1) becomes

$$\begin{aligned} C_{\text{em}}(t) &\propto \langle \Psi_{\text{init}} | \hat{U}_0(-t) \hat{U}_1(t) | \Psi_{\text{init}} \rangle \\ &= \langle \Psi_{\text{init}} | \hat{U}_0(-t) | \Psi_{\text{init}} \rangle e^{-iE_1 t/\hbar}, \end{aligned} \quad (2)$$

where E_1 is the energy of the ground vibrational state of S_1 . Equation (2) states¹⁷ that propagation of the ground vibrational state of S_1 on S_0 determines the correlation function $C_{\text{em}}(t)$, and hence the spectrum, which is obtained via a Fourier transform

$$\sigma(\omega) = A\omega^k \int C_{\text{em}}(t) e^{i\omega t} dt, \quad (3)$$

where $k = 0$ for the line shape and $k = 3$ for the emission spectrum. Prefactor A is a constant factor depending on the type of spectra.^{8,9,18} Since it is constant, in our calculations A was chosen so that the spectra are normalized in the L^∞ norm, i.e., the highest spectral peak is of unit intensity.

B. Thawed Gaussian Approximation

The celebrated *thawed Gaussian approximation*^{16,19} of Heller belongs among the earliest practical semiclassical approaches to quantum dynamics. The main idea is exceedingly simple—since a Gaussian wave packet (GWP) evolving in a globally harmonic potential

retains its functional form, one expects that propagating a single thawed GWP using a local harmonic approximation for the potential can provide a reasonable approximation in many applications, especially when the dynamics of interest is ultrafast. Although the accuracy of the single GWP description is clearly limited, it can provide the most important information beyond that contained in static calculations employing globally harmonic approximation for the potential.^{20,21}

Within TGA, the evolving GWP is assumed in the form

$$\begin{aligned}\psi^t(q) = N^0 \exp\{ - (q - q^t)^T \cdot A^t \cdot (q - q^t) \\ + \frac{i}{\hbar} [p^t \cdot (q - q^t) + \gamma^t] \},\end{aligned}\quad (4)$$

where N^0 is a normalization constant, $x^t = (q^t, p^t)$ denotes the GWP's phase-space center, A^t is a real, symmetric width matrix, and γ^t represents an overall phase factor. Note that γ^t is a time-dependent complex number the imaginary part of which guarantees normalization of $\psi^t(q)$ for $t \geq 0$. The key ingredient of the method consists in expressing the potential $V(q)$ in the *local harmonic approximation* (LHA). This in turn yields a time-dependent effective potential

$$\begin{aligned}V_{\text{eff}}^t(q) = V(q^t) + \nabla V(q^t)^T \cdot (q - q^t) \\ + \frac{1}{2} (q - q^t)^T \cdot \nabla^2 V(q^t) \cdot (q - q^t),\end{aligned}\quad (5)$$

where the potential V , gradient ∇V , and Hessian $\nabla^2 V$ are evaluated at the current coordinate center q^t of the evolving GWP at time t . As already alluded to above, the second-order Taylor expansion (5) ensures that the ansatz (4) is plausible even for $t > 0$. Denoting by

$$H_{\text{eff}}^t := p^T \cdot (G/2) \cdot p + V_{\text{eff}}^t \quad (6)$$

the effective Hamiltonian and inserting the ansatz (4) into the TDSE

$$i\hbar \frac{\partial}{\partial t} \psi^t(q) = H_{\text{eff}}^t \psi^t(q),$$

gives equations of motion for x^t , A^t , and γ^t :

$$\dot{x}^t = \{x, H_{\text{eff}}^t\}, \quad (7a)$$

$$\dot{A}^t = -2i\hbar A^t \cdot G \cdot A^t + \frac{i}{2\hbar} \nabla^2 V(q^t), \quad (7b)$$

$$\dot{\gamma}^t = \mathcal{L}_{\text{eff}}^t - \hbar^2 \text{Tr}[G \cdot A^t], \quad (7c)$$

where G is the inverse of the mass matrix and $\mathcal{L}_{\text{eff}}^t$ denotes Lagrangian dual to H_{eff}^t . Numerical integration of the classical equations of motion (7a) is easily carried out in a symplectic fashion (see Sec. III). In order to integrate Eq. (7b), we follow the strategy¹⁹ proposed by Lee and Heller. Within their method, the matrix A^t is factorized using two auxiliary matrices P^t and Z^t as

$$A^t = \frac{i}{2\hbar} P^t \cdot (Z^t)^{-1}. \quad (8)$$

Since this decomposition is clearly not unique, a further constraint is imposed, namely

$$\dot{Z}^t = G \cdot P^t. \quad (9)$$

In matrix notation, the unique solution of Eqs. (8) and (9) can be written as

$$\begin{pmatrix} P^t \\ Z^t \end{pmatrix} = M^t \cdot \begin{pmatrix} P^0 \\ Z^0 \end{pmatrix}, \quad (10)$$

with initial conditions $Z^0 = I$ and $P^0 = 2i\hbar A^0$. The time-dependent matrix $M^t := \partial x^t / \partial x^0$ is the stability matrix corresponding to the evolving phase-space point x^t . Finally, by inserting Eqs. (8) and (10) into Eq. (7c), and by employing the matrix identity $\det \exp B = \exp \text{Tr } B$, one obtains directly an explicit solution for γ^t in the form

$$\gamma^t = \int_0^t \mathcal{L}_{\text{eff}}^\tau d\tau + \frac{i\hbar}{2} \ln(\det Z^t). \quad (11)$$

Note that since the matrix Z^t is complex, one has to ensure that a proper branch of the logarithm be taken in order to make γ^t continuous in time.

C. On-the-fly *ab initio* TGA

In an OTF-AI (or “direct”) dynamics, the required potential energy surface is generated consecutively at each propagation step by any of the standard electronic structure packages (see Sec. III). In addition to classical trajectory propagation based only on force evaluation, TGA requires to repeatedly evaluate the Hessian $\nabla^2 V$ along the evolving trajectory, since $\nabla^2 V$ is needed²² for propagating the stability matrix M^t .

The evolving GWP is properly defined only in the subspace of the vibrational degrees of freedom of the molecule of interest. Therefore, a germane choice of the coordinate system is essential. We illustrate the procedure employed in the numerical calculations on a specific

scenario of two, ground and excited PESs, where the initial GWP corresponding to the ground vibrational state of the excited electronic PES is subsequently propagated on the ground electronic surface. Let us consider a reference equilibrium geometry ξ_{ref} on the excited PES, where ξ_{ref} is a vector with $3N$ Cartesian components, with N denoting the number of atoms in the molecule. Any displaced molecular configuration ξ , obtained, e.g., by propagation on a different PES, can be related to the normal-mode coordinates η as

$$\xi - \xi_{\text{ref}} = G^{\frac{1}{2}} \cdot O \cdot \eta = T \cdot \eta, \quad (12)$$

with $T := G^{\frac{1}{2}} \cdot O$ and O denoting the orthogonal matrix that diagonalizes the mass-scaled Cartesian Hessian matrix evaluated at ξ_{ref} , i.e., $T^T \cdot \nabla^2 V|_{\xi_{\text{ref}}} \cdot T = \Omega^2$, where $\Omega = \text{diag}(\omega_1, \dots, \omega_{3N})$ is the diagonal matrix containing the normal-mode frequencies. Note that η in Eq. (12) has $3N$ components, i.e., incorporates also the 3 translational and 3 rotational degrees of freedom. The initial values of these displacements are zero and one would like to preserve this constraint also during the dynamics on the ground PES. The translational modes are projected out easily by shifting the center of mass to the origin of the Cartesian frame. Next, in order to minimize the coupling to the remaining 3 rotational modes, we closely follow the axis-switching procedure devised by Hougen and Watson.^{23,24} In this spirit, any displaced configuration ξ is rotated relatively to ξ_{ref} in order to satisfy Eckart's conditions:

$$\sum_{a=1}^N m_a (P_a \cdot \xi_{\text{ref}}) \times [P_a \cdot (\Lambda \cdot \xi)] = 0. \quad (13)$$

In Eq. (13), the sum runs over all N atoms, Λ is a $3N \times 3N$ block-diagonal matrix, where each of the N blocks is a copy of a 3-dimensional rotation matrix R , and the $3 \times 3N$ matrix P_a is defined as $(P_a)_{i,j} = \delta_{i,1}\delta_{j,3a-2} + \delta_{i,2}\delta_{j,3a-1} + \delta_{i,3}\delta_{j,3a}$. Application of P_a to a configuration ξ essentially selects coordinates of the a th atom. Having minimized the coupling to the rotational modes, one can afford to consider in Eq. (12) only the first $(3N - 6)$ columns of the matrix O . In that case, the transformation matrix T also reduces to a $3N \times (3N - 6)$ form. Kudin and Dymarsky showed²⁵ that the rotation matrix R solving Eq. (13) can be obtained by minimizing the mass-weighted root-mean-square distance of ξ with respect to the reference configuration ξ_{ref} . In practice, this is achieved efficiently, e.g., by employing direct methods based on singular value decomposition or quaternion formalism.²⁶

The transformation from the Cartesian to the vibrational normal-mode coordinates is thus performed in three consecutive steps. First, the configuration ξ is shifted to the center-

of-mass system. Second, it is rotated to the Eckart frame, and finally it is projected onto the vibrational normal modes, i.e.,

$$\eta = W \cdot [\Lambda \cdot (\xi - \Delta) - \xi_{\text{ref}}], \quad (14)$$

where $W := T^T \cdot G^{-1}$ and the center-of-mass vector Δ is defined as

$$\Delta := \left(\sum_{a=1}^N P_a \right)^T \cdot \sum_{a=1}^N m_a P_a \cdot \xi / \sum_{a=1}^N m_a. \quad (15)$$

Finally, one also needs to express the Cartesian force $\nabla_\xi V$ and the Cartesian Hessian matrix $\nabla_\xi^2 V$ in the η -coordinates:

$$\nabla_\eta V = (W \cdot \Lambda) \cdot \nabla_\xi V, \quad (16a)$$

$$\nabla_\eta^2 V = (W \cdot \Lambda) \cdot \nabla_\xi^2 V \cdot (W \cdot \Lambda)^T. \quad (16b)$$

D. Stability matrix propagation: Symplecticity and effect of Hessian interpolation

The GWP's center and the accompanying stability matrix M^t are propagated classically using the second-order symplectic algorithm.²² Propagation of M^t is the most expensive part of the entire OTF-AI calculation since it requires knowledge of the Hessian of the PES along the evolving trajectory.

The associated computational costs can be alleviated by employing a Hessian update scheme, within which the Hessian is evaluated directly only once every $s \geq 1$ steps and approximated at the remaining steps with an extrapolation method requiring gradients. Note that these Hessian update schemes are in the context of dynamics typically used for the propagation of the classical trajectory itself, e.g., within the framework of higher-order predictor-corrector schemes (see Refs. 27 and 28 and references therein). In contrast, in Refs. 12, 29, and 30 as well as in the present work, approximative treatment of the Hessian is used only for the propagation of M^t . However, whereas in Refs. 12, 29, and 30 the Hessian update is based on extrapolation, in this work polynomial interpolation of order b is used to obtain the Hessian at intermediate steps. A Hessian extrapolation update scheme would be convenient in cases for which analytical *ab initio* Hessians are not available, e.g., for absorption spectrum calculation.

Note that our approach requires propagating the full classical trajectory and storing the necessary information regarding the potential first, and interpolating the Hessian later. The TGA GWP is computed in the second pass through the stored data. The advantage of this approach is twofold: First, the independent Hessian calculations in the second pass are easily parallelized. Second, one can perform a global analysis of the trajectory over the entire propagation range (see Subsec. II E).

As the first test, we check the conservation of the *symplectic condition*

$$M^{t\top} \cdot J \cdot M^t = J \quad (17)$$

by the $2D \times 2D$ stability matrix M^t , where J is the standard symplectic matrix

$$J := \begin{pmatrix} 0_D & I_D \\ -I_D & 0_D \end{pmatrix}$$

and I_D is the D -dimensional identity matrix. The deviation from Eq. (17) is evaluated in terms of the error

$$\epsilon^t := \|M^{t\top} \cdot J \cdot M^t - J\|_F, \quad (18)$$

where $\|A\|_F := \sqrt{\text{Tr}(A^\top \cdot A)} = \sqrt{\sum_{i=1}^{2D} \sum_{j=1}^{2D} |A_{ij}|^2}$ denotes the Frobenius norm³¹ of matrix A and the exact stability matrix satisfies

$$\epsilon^t = 0. \quad (19)$$

For instance, in the T2 calculation, Eq. (19) is well satisfied even for Hessian interpolated from AI values computed only every 2, 4, 8, or 16 steps. For details see Fig. 1(a) in the Supplementary Material.³² It is important to note that any violations of Eq. (19) are due to round-off errors, since in an infinite-precision arithmetics, Eq. (19) would be satisfied even if the true Hessian were replaced by an arbitrary symmetric matrix \mathcal{H}^t . The only additional requirement is that M^t be propagated symplectically,²² since the symmetry of \mathcal{H}^t is guaranteed by the interpolation algorithm. Incidentally, note that Eq. (19) is much more stringent than the widely used Liouville condition, which only requires conservation of the phase-space volume, expressed by the requirement $\det(M^{t\top} \cdot M^t) = 1$, and automatically follows from symplecticity [Eq. (19)].

The influence of the interpolation procedure with $s > 1$, $b \geq 0$ on the GWP evolved with the TGA is quantified in terms of fidelity—a quantity introduced by Peres³³ to measure

sensitivity of quantum dynamics to perturbations. In our setting, the fidelity is defined as the squared magnitude of the time-dependent overlap of GWP_s propagated using the TGA with and without interpolation:

$$F_{s,b}(t) := |\langle \psi_{1,b}^t | \psi_{s,b}^t \rangle|^2. \quad (20)$$

In the T2 case, e.g., interpolating every four steps using the second order interpolation ($b = 2$) has almost no effect on the propagated GWP, while the OTF-AI calculation is accelerated almost four times [see Fig. 1(b) in the Supplementary Material³²].

E. Identification of the essential DOFs

Perhaps the greatest advantage of trajectory-based methods is the possibility to visualize the dynamics and directly study its influence on the resulting spectra. However, direct analysis can become quite cumbersome for systems of high dimensionality. Moreover, the dynamical couplings among individual degrees of freedom (DOFs) pose additional complications since all the coupled DOFs must be analyzed simultaneously. In this subsection, we introduce a particular approach for extracting the essential characteristics of the dynamics of a generic system with D vibrational DOFs. To some extent, this method shares common grounds with other “effective modes” techniques aspiring to identify the modes responsible for the main spectral features, e.g., methods tailored for the description of nonadiabatic transitions.³⁴ However, in contrast to Ref. 34, the identification of the essential DOFs is here performed on the fly. The “tool” proposed here is used in Subsec. IV B for analyzing and interpreting the emission spectra of the oligothiophene T_n family.

In order to simplify the discussion below, we introduce the symbol \mathcal{D} to denote the space spanned by all D DOFs. Any subspace of \mathcal{D} is then identified with the subset of indexes of those DOFs that span the given subspace. In this spirit, \mathcal{D} itself is identified with the set $\mathcal{D} = \{1, 2, \dots, D\}$. Note that the set of normal mode coordinates provide a natural physical realization of \mathcal{D} , nevertheless our approach is not limited to this particular choice.

Briefly put, our strategy is as follows. First, we decompose the set \mathcal{D} of all vibrational DOFs into mutually disjoint subsets, where the DOFs in different subsets can be thought of as approximately dynamically independent. Second, we identify the dynamically most important DOFs and then consider only those subsets of \mathcal{D} which contain at least one of these “important” DOFs.

To quantify the coupling between various DOFs, we utilize the stability matrix to measure the *information flow* among individual DOFs. The “flow” B_{ij} between i th and j th DOF is then defined as

$$B_{ij} := \left| \frac{\beta_{ij}}{\beta_{ii}} \right|, \text{ with } \beta := \frac{1}{T} \int_0^T dt \kappa^\top \cdot \tilde{M}^t \cdot \kappa, \quad (21)$$

where $\tilde{M}_{ij}^t = |M_{ij}^t|$ and $\kappa^\top = (I_D, I_D)$ denotes a two-component vector, each component of which is a D -dimensional identity matrix. The value of β_{ij} is rescaled in Eq. (21) by $1/\beta_{ii}$ in order to make the diagonal elements unital ($B_{ii} = 1$), as in uncoupled systems, and to focus solely on the coupling effects among different DOFs ($i \neq j$). For connection to and comparison with the analysis based on the global harmonic model or Duschinsky matrix, we refer to Sec. G of the Supplementary Material.³²

The decomposition of \mathcal{D} into (approximately) dynamically decoupled subsets of DOFs is then constructed by means of the concept of ε_B -partitioning:

$$\mathcal{D} = \bigcup_{\alpha=1}^{\bar{c}(\mathcal{D}, \varepsilon_B)} \mathcal{D}_\alpha^{\varepsilon_B}, \quad (22)$$

where $\bar{c}(\mathcal{D}, \varepsilon_B)$ denotes the number of mutually disjoint subsets $\mathcal{D}_\alpha^{\varepsilon_B}$ defined as the maximal connected components of an undirected graph with adjacency matrix³⁵

$$E_{ij} := \begin{cases} 1 & \text{if } \max\{B_{ij}, B_{ji}\} \geq \varepsilon_B, \\ 0 & \text{otherwise,} \end{cases} \quad (23)$$

with a particular threshold value ε_B .

Any nontrivial decomposition (22), where each subset $\mathcal{D}_\alpha^{\varepsilon_B}$ is interpreted as uncoupled, yields a partially separable dynamics. Depending on the value $\bar{c}(\mathcal{D}, \varepsilon_B)$, this separation can significantly reduce computational costs, since the total correlation function can be obtained as a product of individual contributions evaluated independently on each subspace (i.e., subset $\mathcal{D}_\alpha^{\varepsilon_B}$).

Next, we identify the set $\mathcal{G}^{\varepsilon_\varrho} \subseteq \mathcal{D}$ of the dynamically most important DOFs. For this purpose, we employ the *relative displacement* vector ϱ , the i th component of which is defined as the maximal relative displacement in the coordinate ς_i , describing the i th DOF, where the maximum is understood to be taken over the total propagation range $[0, T]$, i.e.,

$$\varrho_i := \max_{0 \leq t \leq T} |\varsigma_i^t| (A_{ii}^0 / \ln 2)^{1/2} \text{ for } 1 \leq i \leq D. \quad (24)$$

Here, the scaling factor containing the diagonal element A_{ii}^0 of the width matrix of the initial GWP ensures that the spread of the nuclear wave function be taken into account: A small displacement of a high-frequency (stiff) mode modulates the correlation function much more than the same displacement of a low-frequency (soft) mode. The set $\mathcal{G}^{\varepsilon_\varrho}$ of dynamically most important modes is then defined by

$$i \in \mathcal{G}^{\varepsilon_\varrho} \Leftrightarrow \varrho_i \geq \varepsilon_\varrho, \quad (25)$$

where ε_ϱ is a prescribed threshold value. A particular DOF is thus interpreted as “dynamically important” if the dynamics displaces it sufficiently relative to the width of the initial vibrational state.

Finally, we combine the two ideas, i.e. the decoupling based on the ε_B -partitioning [Eq. (22)], and the selection of important modes based on the relative displacement ϱ [Eq. (24)], to form an “active space” $\mathcal{A}^{\varepsilon_B, \varepsilon_\varrho}$ comprised of all subsets $\mathcal{D}_\alpha^{\varepsilon_B}$ containing at least one dynamically important DOF from $\mathcal{G}^{\varepsilon_\varrho}$:

$$\mathcal{A}^{\varepsilon_B, \varepsilon_\varrho} = \bigcup_{\alpha \in \mathcal{S}} \mathcal{D}_\alpha^{\varepsilon_B}, \text{ with } \mathcal{S} := \{\beta : \mathcal{G}^{\varepsilon_\varrho} \cap \mathcal{D}_\beta^{\varepsilon_B} \neq \emptyset\}. \quad (26)$$

Note that the number $c(\mathcal{D}, \varepsilon_B, \varepsilon_\varrho) := |\mathcal{S}|$ of contributing subsets $\mathcal{D}_\alpha^{\varepsilon_B}$ is in general smaller than $\bar{c}(\mathcal{D}, \varepsilon_B)$ of Eq. (22). In order to obtain a contiguous labeling of the subsets in decomposition (26), we introduce a bijective (but otherwise arbitrary) mapping l between sets \mathcal{S} and $\{1, \dots, c(\mathcal{D}, \varepsilon_B, \varepsilon_\varrho)\}$. This allows to restate Eq. (26) as

$$\mathcal{A}^{\varepsilon_B, \varepsilon_\varrho} = \bigcup_{\alpha=1}^{c(\mathcal{D}, \varepsilon_B, \varepsilon_\varrho)} \mathcal{A}_\alpha^{\varepsilon_B, \varepsilon_\varrho}, \text{ where } \mathcal{A}_\alpha^{\varepsilon_B, \varepsilon_\varrho} := \mathcal{D}_{l(\alpha)}^{\varepsilon_B}. \quad (27)$$

The subsets $\mathcal{A}_\alpha^{\varepsilon_B, \varepsilon_\varrho}$ are in the following referred to as *groups*. (Mathematically, these “groups” are just “sets” and should not be confused with a precise mathematical notation of group.)

In summary, individual DOFs are by definition considered to be coupled only within groups the union of which forms the space $\mathcal{A}^{\varepsilon_B, \varepsilon_\varrho}$. Each group then contains at least one DOF classified as dynamically important on the basis of the rule (25). The total number of groups $c(\mathcal{D}, \varepsilon_B, \varepsilon_\varrho)$ and their structure is mainly determined by the values of the two thresholds ε_ϱ and ε_B which have to be chosen appropriately according to the system and process of interest.

Let us now demonstrate the approach outlined above on one particular example of T2, the dithiophene molecule. Since an oligothiophene T_n is comprised of

$$N(n) = 7n + 2 \quad (28)$$

atoms, the space \mathcal{D} is of dimensionality $D(n) := 3N(n) - 6 = 21n$, i.e., in the case of T2 ($n = 2$), there are 42 vibrational DOFs. To be explicit, these vibrational DOFs are identified with normal-mode coordinates of PES S_1 . Individual modes are in Fig. 1 represented by colored circles with juxtaposed vibrational frequencies. Now, for $\varepsilon_B = 0.045$, one obtains 4 subsets in the decomposition (22), i.e., $\bar{c}(\mathcal{D}, \varepsilon_B) = 4$. Further, we identify the set of important modes \mathcal{G} using rule (25). With threshold value $\varepsilon_\varrho = 0.6$, we isolate 8 modes, i.e., $|\mathcal{G}^{\varepsilon_\varrho}| = 8$. These modes are shown in red color in Fig. 1. Finally, we see that for this choice of the thresholds, we obtain only one group in the decomposition (27) since $\mathcal{G}^{\varepsilon_\varrho} \cap \mathcal{D}_\beta^{\varepsilon_B} \neq \emptyset$ only for $\beta = 1$. Thus $c(\mathcal{D}, \varepsilon_B, \varepsilon_\varrho) = 1$ and the bijective mapping l is merely an identity.

In practical calculations, ε_ϱ and ε_B must be chosen carefully. For high threshold values ε_B , one can profit from an approximate separability of the model. However, too high values of either ε_B or ε_ϱ might yield inaccurate results.

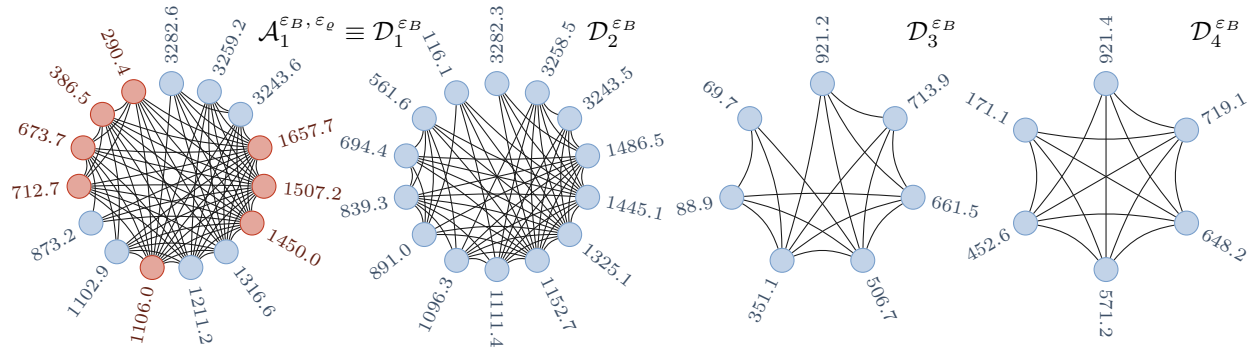


Figure 1. Partitioning of S_1 normal-mode coordinates of dithiophene T2 into approximately independent subsets for the threshold value $\varepsilon_B = 0.045$ [see Eq. (22)]. Colored circles represent individual modes, i.e., elements of \mathcal{D} . The dynamically important modes [Eq. (25)] comprising $\mathcal{G}^{\varepsilon_\varrho}$ with the threshold value $\varepsilon_\varrho = 0.6$ are shown in red. Finally, solid lines represent inter-mode couplings above the threshold ε_B . Vibrational frequencies are given in cm^{-1} .

III. COMPUTATIONAL DETAILS

All *ab initio* calculations were performed with the Gaussian09 package.³⁶ Its output was extracted directly from the checkpoint file. The ground PES (S_0) was handled with the density functional theory (DFT), whereas the first excited singlet PES (S_1) was described with the time-dependent DFT (TD-DFT). Following the work of Stendardo *et al.*, our TD-DFT calculations were based on the long-range corrected CAM-B3LYP functional¹¹ with 6-31+G(d,p) basis set. Within this TD-DFT setup, the energy gap between the S_0 and S_1 PESs of oligothiophenes is described quite accurately. Although Gaussian09 provides analytical gradients for both DFT and TD-DFT, analytical Hessians are available only for DFT. No symmetry constraints were enforced and the “fine” and “ultra fine” integration grids were used for OTF-AI calculations and geometry optimization, respectively.

In order to find the physically relevant equilibrium geometry of S_1 for each oligothiophene T_n , we first performed an S_0 geometry optimization of the “all-trans” conformer, the rings of which are oriented in an anti conformation with respect to their neighbors. The work by Becker and co-workers² suggests that this is the most stable conformer. The S_1 geometry optimization was started from this S_0 equilibrium geometry. It has been well-established that in contrast to the inter-ring twisted S_0 equilibrium geometry and its shallow potential, S_1 exhibits a steep, deep, harmonic-like well in the vicinity of its planar equilibrium geometry.^{2,37} The S_1 equilibrium geometry, shown in the Supplementary Material,³² served as the reference structure for the OTF-AI-TGA dynamics.

Within the OTF-AI-TGA, the GWP was propagated for the total time of 7976 a.u. \approx 193 fs with a time step of 8 a.u. \approx 0.2 fs using the second order symplectic algorithm. The resulting spectra were subjected to a phenomenological (inhomogeneous) Gaussian broadening with half-width at half-maximum (HWHM) of 0.025 eV \approx 200 cm⁻¹.

IV. RESULTS AND DISCUSSION

A. Comparison with experimental spectra

Our results confirm the utility of the OTF-AI-TGA approach for electronic spectra calculation, since all important features of the experimental spectra are almost perfectly reproduced. Figure 2 demonstrates the agreement with the overall shape, peak intensities, as

well as the trend of the spectra to gradually shift towards lower frequencies with increasing number of rings in the molecule. Note that particular experimental conditions, notably the interaction with the solvent (here, ethanol glass at 77 K), can produce a shift of the spectrum. However, we disregard this effect since the resulting shift is expected to be small for a broad class of solvents.^{2,37,38} Also, the exact prediction of the spectrum position is partly beyond the level of the *ab initio* setup employed here (see Sec. III).

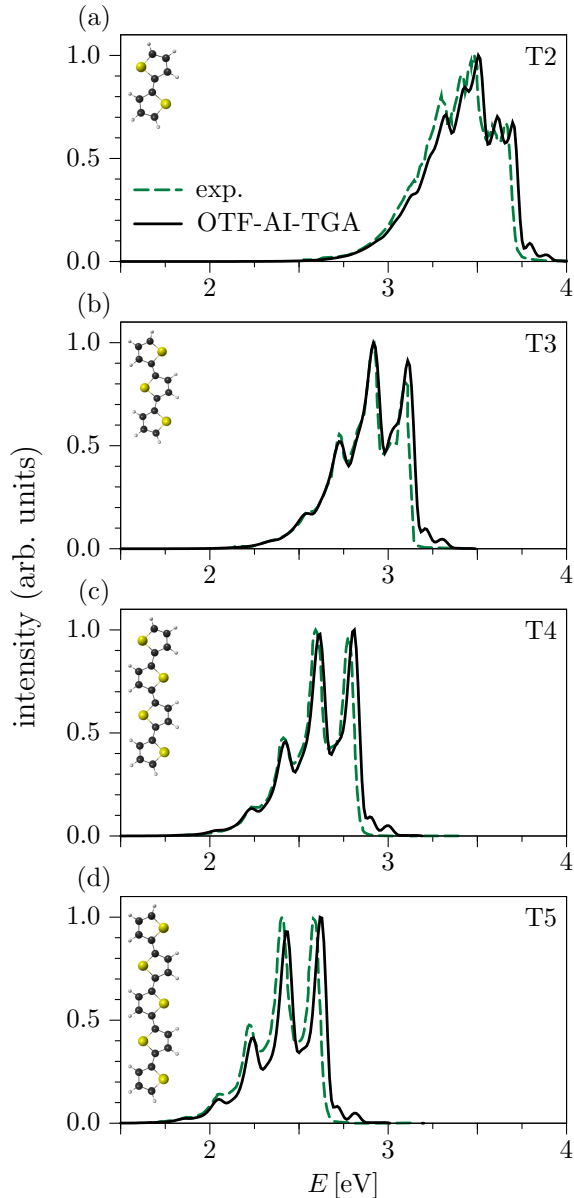


Figure 2. Emission spectra of the oligothiophene T_n family for $n \in \{2, 3, 4, 5\}$: Comparison of experimental emission spectra (exp., dashed green line) with the full-dimensional OTF-AI-TGA calculations using all $21n$ normal modes (solid black line).

Becker *et al.*³⁹ reported a significant red shift of the oligothiophene absorption spectra at low temperatures and attributed this phenomenon to the twisted \leftrightarrow planar conformational transition induced by solvent freezing. Interestingly, this shift was not observed in the emission spectra, which suggests that in the whole temperature range it is only the planar conformation that plays a significant role in this process. Even without imposing explicit planarity constraints, no deviations from the planar conformation were observed during the ground-state gas-phase OTF-AI dynamics due to planarity of the initial geometry. This fact makes the comparison of our gas-phase results to the experimental data more legitimate. Finally note that the *ab initio* ground state equilibrium geometry is twisted in contrast to the equilibrium geometry in ethanol glass at 77 K. Therefore, the $n - 1$ torsional degrees of freedom connecting the planar and twisted geometries of T_n have imaginary frequencies. Since our approach is unable to describe wave-packet splitting, the TGA GWP only spreads along these degrees of freedom (see Supplementary Material,³² Sec. E). However, since we are mainly interested in short-time dynamics, this behavior is qualitatively correct. Hence, the OTF-AI-TGA approach remains in this case robust even for floppy molecules and the question about the “harmonicity” of the system is of much lesser importance due to the employment of the local harmonic approximation. Although the global harmonic approximation is quite adequate for T_n,¹¹ small changes of the peak positions and intensities can be observed as compared to OTF-AI-TGA (see Supplementary Material,³² Sec. F).

To facilitate comparison between line-shape spectra of oligothiophenes with different numbers of thiophene rings, the spectra shown in Fig. 3(a) are first L^∞ normalized and subsequently shifted so that the “ α_0 -peaks” overlap at zero energy. This reveals that the relative peak positions are rather insensitive to n , while their prominence is increasing with increasing n . The peak at the highest energy (in our notation: α_0) in the emission spectrum is attributed to the 0–0 transition.⁴⁰ The position of the α_1 -peak is close to the vertical transition energy E_{vert} , which, in loose terms, justifies its dominance in Fig. 3(a). More detailed classification of individual spectral peaks into the α, β groups and their interpretation from the dynamical viewpoint is discussed in Subsec. IV B.

It has been found experimentally that the 0–0 transition energy E_{0-0} in the polythiophene family T_n is a linear function of $1/n$.^{2–5} In accordance with this observation and our identification of E_{0-0} with E_{α_0} , we found that E_{α_0} is accurately described by the function $E_{\alpha_0}(n) \approx (3.58/n + 1.91)$ eV. Good agreement with the experiment can be directly inferred

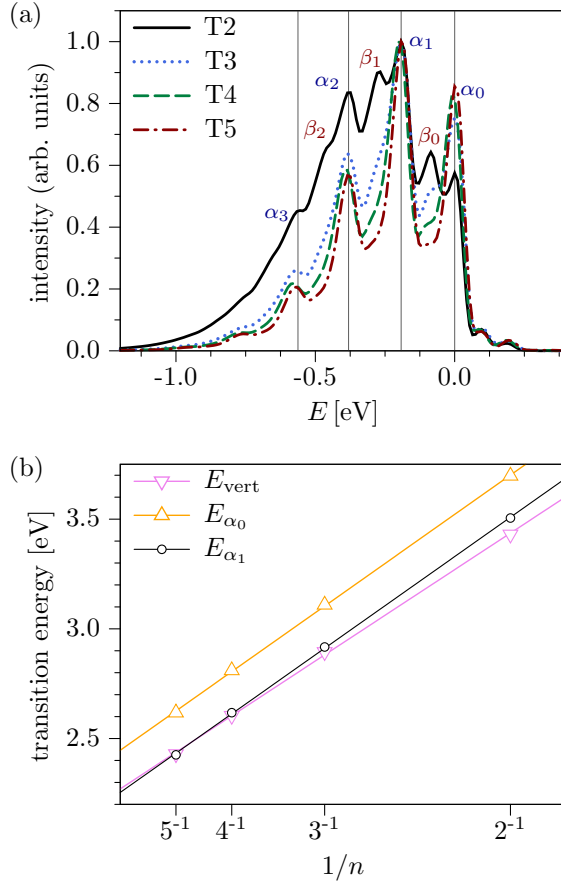


Figure 3. Emission in the oligothiophene T_n family for $n \in \{2, 3, 4, 5\}$. (a) L^∞ -normalized line-shape spectra. To facilitate their comparison, the spectra are shifted independently for each n so that the α_0 peak appears at zero energy. (b) Dependence of the vertical-transition energy E_{vert} and positions of the α_0 and α_1 -peaks (E_{α_0} , E_{α_1}) on $1/n$ (see text for details). Linear fits are denoted with lines.

from Fig. 2. Furthermore, from the *ab initio* data, we determined in a similar fashion that $E_{\text{vert}}(n) \approx (3.33/n + 1.77)$ eV. Fits of E_{α_0} , E_{α_1} and E_{vert} are shown in Fig. 3(b).

Note that the relative intensity of the α_0 -peak, identified with the 0–0 transition, in Fig. 3(a) increases with n . This can be related to the fact that the slope of $E_{\alpha_1}(n)$ is larger than the slope of $E_{\text{vert}}(n)$ [see Fig. 3(b)], using the following heuristic argument: Neglecting the difference between the S_0 and S_1 zero-point energies, the 0–0 transition energy depends solely on the energy gap between these PESs. On the other hand, E_{vert} is influenced also by the relative displacement of the S_0 and S_1 potential minima. Therefore, if E_{vert} decreases more slowly with increasing n than does the 0–0 transition energy, one can expect a decrease

not only in the energy gap between S_0 and S_1 PESs but also in the relative displacement of their minima, which, in turn, is responsible for the gain in intensity of the 0–0 transition, i.e., the α_0 -peak. This observation is in agreement with the Huang-Rhys analysis performed by A. Yang *et al.*⁴ on fluorescence spectra of Tn for $n \in \{3, 4, 5, 6\}$.

B. Vibrational analysis

To gain a deeper understanding of the emission spectra shown in Figs. 2 and 3, we employ independently for each oligothiophene Tn the analysis proposed in Subsec. II E adapted to the normal-mode coordinates of the S_1 PES of Tn . To this end, we closely follow the example presented at the end of Subsec. II E. The normal-mode classification based on decompositions (27) and (29) with $\varepsilon_B = 0.55$ and $\varepsilon_\rho = 0.6$ results for all Tn in an active space \mathcal{A} comprised of six groups of modes (see Tab. I). This space is spanned by ten “active” modes (i.e., $|\mathcal{A}| = 10$) for $T2-T4$, while $|\mathcal{A}| = 8$ for $T5$. The thresholds were chosen in order to obtain a minimal set \mathcal{A} of active modes with as many subsets as possible on condition that the reduced OTF-AI-TGA spectrum $\sigma_{\mathcal{A}}$ recovers all important features of the “complete” spectrum $\sigma_{\mathcal{D}}$. For clarity, the subscript of σ denotes explicitly the set of modes taken into account in the spectra calculation. Formally, the spectrum $\sigma_{\mathcal{A}}$ can be thought of as the computationally cheapest, yet still sufficiently accurate approximation of $\sigma_{\mathcal{D}}$.

For details regarding correlation function and spectra calculations within proper subspaces of \mathcal{D} we refer to the Appendix A. From now on, to simplify notation, the implicit dependence of, e.g., \mathcal{A} on the threshold values ε_B and ε_ρ will not be denoted explicitly.

Figure 4(a) demonstrates that ten modes were sufficient to essentially reproduce the complete spectrum $\sigma_{\mathcal{D}}$ for $T2$. The simplification achieved is the most striking for $T5$ [Fig. 4(b)], for which eight modes were sufficient and hence the dimensionality was reduced more than ten times without losing any major feature in the spectrum. However, note that the “ $|\mathcal{A}|$ -mode” spectra in Fig. 4 are slightly shifted due to dependence of the zero-point energy on the choice of \mathcal{A} . (Analogous spectra of $T3$ and $T4$ are shown in Sec. B of the Supplementary Material.³²)

The modes in \mathcal{A} are by definition considered to be coupled only within individual groups. Therefore, one can attempt to assign a characteristic vibrational movement of the entire molecule induced by excitation of the modes belonging to a particular group. Among the

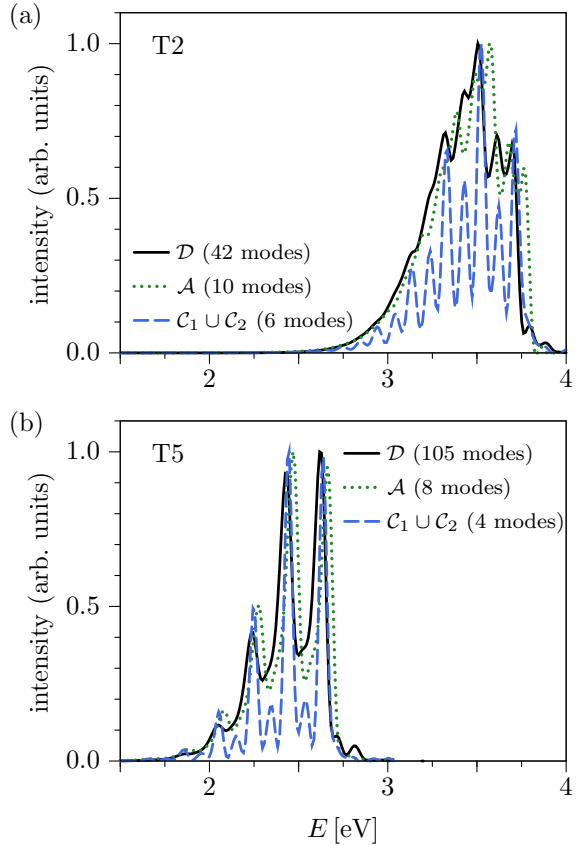


Figure 4. Emission spectra of oligothiophenes T2 (a) and T5 (b): comparison of the full-dimensional OTF-AI-TGA spectrum σ_D (solid black line) with the spectrum σ_A (dotted green line) computed within the subspace \mathcal{A} of the active modes and the spectrum $\sigma_{C_1 \cup C_2}$ (dashed blue line) taking into account only modes belonging to the classes C_1 and C_2 (see Fig. 6 and Tab. I) introduced in Eq. (29).

24 groups ($24 = 4$ oligothiophenes \times 6 groups per oligothiophene), we identified 7 characteristic motions shown on the examples of T3 and T4 molecules in Fig. 5. In Table I, these characteristic motions are distinguished with a superscript.

Next, the six groups of normal modes are, for each $n \in \{2, 3, 4, 5\}$, merged into three disjoint *classes* C_1 , C_2 , and C_3 as

$$C_1 := \mathcal{A}_1, \quad C_2 := \mathcal{A}_2, \quad \text{and} \quad C_3 := \bigcup_{\alpha=3}^6 \mathcal{A}_\alpha. \quad (29)$$

The reason for introducing an additional logical layer is the observation in Fig. 6 that the overall character of the spectrum σ_{C_i} corresponding to the i th group is only mildly influenced by n , whereas the dependence on i is dominant. In loose terms, the first group C_1 comprises inter-ring stretch modes and is mainly reflected in the “ α -peaks” of the complete spectrum

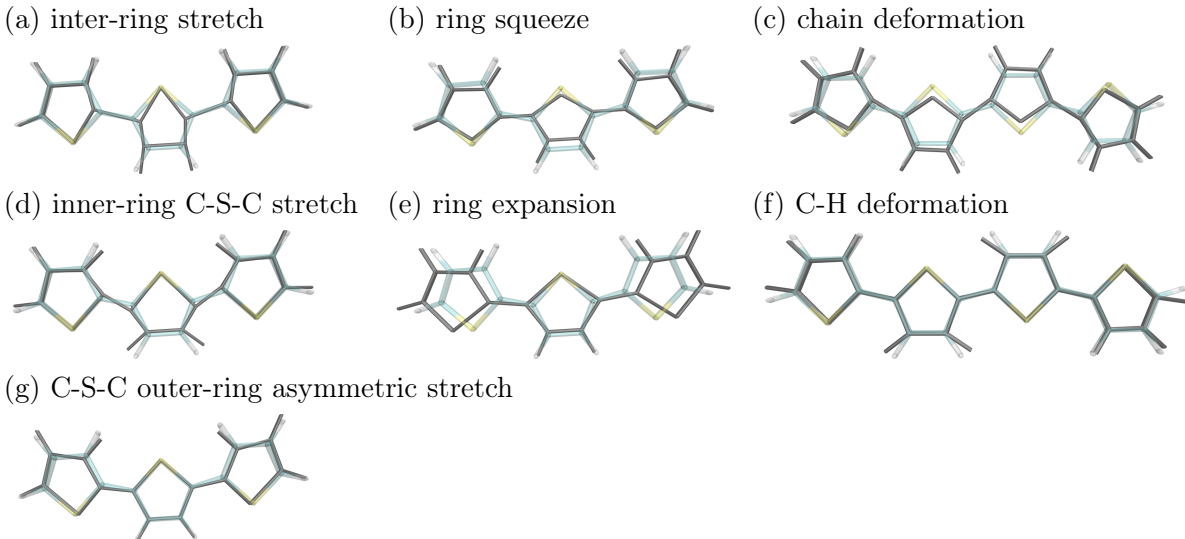


Figure 5. Characterization of the active normal modes in the set $\mathcal{A} \subseteq \mathcal{D}$ [see Eqs. (27) and (29)] by the nature of the deformation which they exert on the oligothiophene T_n skeleton. To cover all cases presented in Tab. I, these deformations are shown on the examples of T_3 and T_4 . Panel labels correspond to the classification in Tab. I.

$\sigma_{\mathcal{D}}$ [see Fig. 3(a)]. The second group \mathcal{C}_2 consists of a ring-squeeze mode and produces the “ β -peaks” in Fig. 3(a). Finally, the modes contained in the third group cause merely an overall broadening of the spectrum. Such a classification of vibrational modes, essential for a theoretical interpretation of the emission spectra, is also useful in practice, e.g., in the design of organic light-emitting diodes (OLEDs).⁴¹

The difference between individual classes is further emphasized by introducing an “overall relative displacement” of the i th class as $R_i^2 := \sum_{j \in \mathcal{C}_i} \varrho_j^2$. We have found that R_1 is highly correlated with $-n$ while R_2 with $1/n$. Therefore, for low n , the dynamical importance of the class \mathcal{C}_2 decreases faster with increasing n . This results in less structured spectra, shown in Fig. 3(b), in which the β -peaks are almost invisible already for T_3 .

In summary, the inter-ring stretch motion is seen to have a dominant effect on the T_n spectra, especially for $n > 2$. Comparing the relative displacements of the classes \mathcal{C}_1 and \mathcal{C}_2 helps to further corroborate the hypothesis (stated above) that the S_0 and S_1 geometries become less displaced with increasing n since the 0–0 transition energy $E_{0-0}(n)$ decreases faster than the vertical excitation energy $E_{\text{vert}}(n)$.

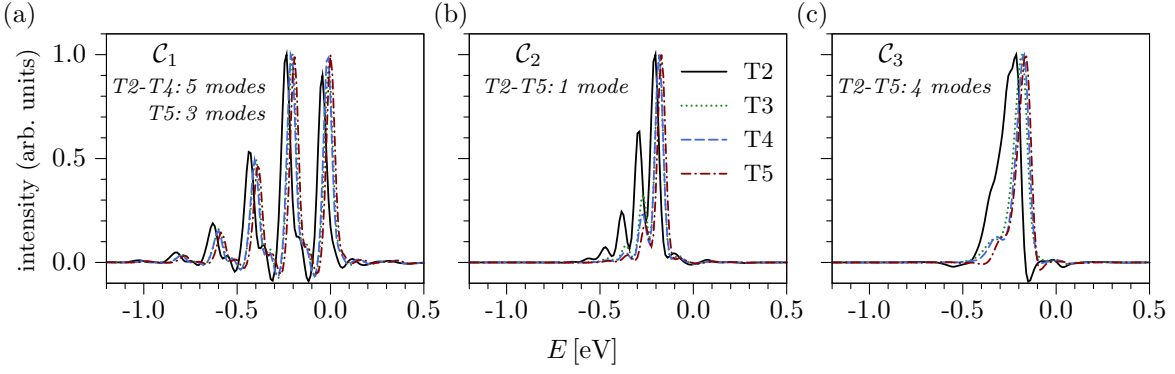


Figure 6. Classification of normal modes of the oligothiophene T_n family according to their influence on the resulting emission spectrum [see Eqs. (27) and (29)]. Detailed description of individual classes is contained in Tab. I. (a) Inter-ring stretch modes responsible for the α -peaks shown in Fig. 3. (b) Ring-squeeze mode reflected in the β -peaks in Fig. 3. (c) Remaining modes causing overall broadening of the spectra.

C. Quinoid structure of S_1

The extent of π -conjugation along the oligomer chain is reflected in the quinoid structure of individual rings. The degree of the quinoid/aromatic character of the i th ring in T_n can be quantified in terms of the so-called *bond length alternation*^{42–44} (BLA)

$$\text{BLA}_i = R_{\beta_i} - (R_{\alpha_i} + R_{\alpha'_i})/2, \quad (30)$$

where R denotes the length of the β , α , and α' bonds of the i th ring (see Fig. 7). Hence, quinoid rings have a negative BLA, while aromatic rings have a positive BLA.

The S_1 equilibrium geometries of T_n in Fig. 7 reveal that for $n > 2$, both quinoid and aromatic ring types are present in the chain: The inner rings are quinoid, while the end rings are aromatic. On the other hand, both rings of T_2 have quinoid character. However, the large difference between the lengths of α and α' bonds suggests a double-bond character of the outer α bond in T_2 . In general, the DFT S_1 geometries exhibit more pronounced quinoid character in comparison with the S_1 geometries calculated at the MNDO level,⁴² which describe T_2 as slightly aromatic.

The time dependence of BLA, displayed for T_5 in Fig. 8 and for T_2 , T_3 , and T_4 in Sec. C of the Supplementary Material,³² shows emission-induced oscillations between the quinoid and aromatic characters of individual rings. The inner rings are seen to be subjected to

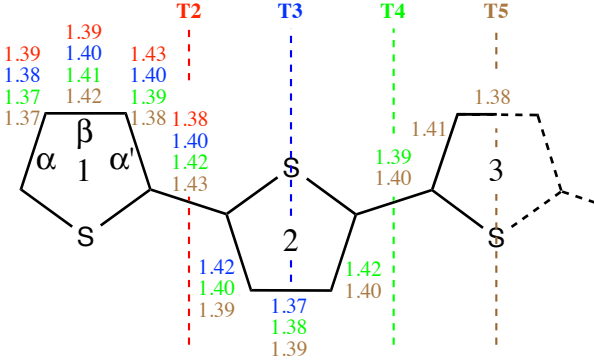


Figure 7. Equilibrium S_1 geometry of oligothiophenes T_n for $n \in \{2, 3, 4, 5\}$. Corresponding bond lengths for different oligothiophenes T_n are juxtaposed with each other next to individual bonds, whereas the dashed lines represent the end of the half-chain for each T_n . E.g., to the right of the dashed line marked as T_3 there are only one or two bond-length values since those bonds are not present in the half-chain of T_2 and T_3 .

larger structural variations, while the outer rings remain aromatic, although the degree of aromaticity changes periodically. Hence, the quinoid character of T_n in S_1 is well localized over just 2-3 rings, as was shown also by Beljonne *et al.*,⁴² while the emission process triggers deformation of the whole chain.

Oligomer vibrational line shapes are usually analyzed in terms of the effective conjugation coordinate^{45–47} (ECC)—a totally symmetric internal coordinate describing the variation of adjacent C-C backbone stretches, responsible for the change from the aromatic to quinoid structure. A detailed analysis (summarized in Appendix B) of the dynamics shows that only some of the modes coupled to ECC are also excited by the fluorescence process. The overall contribution of the A_1 group to the ECC is more than 92% for all oligothiophenes and, hence, the α -peaks originate from the change of the ECC during the dynamics induced by the fluorescence process.

V. CONCLUSION

All features of the experimental emission spectra of oligothiophenes with up to five rings (i.e., up to 105 vibrational DOFs) are well reproduced by our OTF-AI-TGA calculations. The efficiency of the TGA formulation is found to allow treating all vibrational DOFs on an equal footing even in case of larger systems especially since the OTF-AI scheme does not

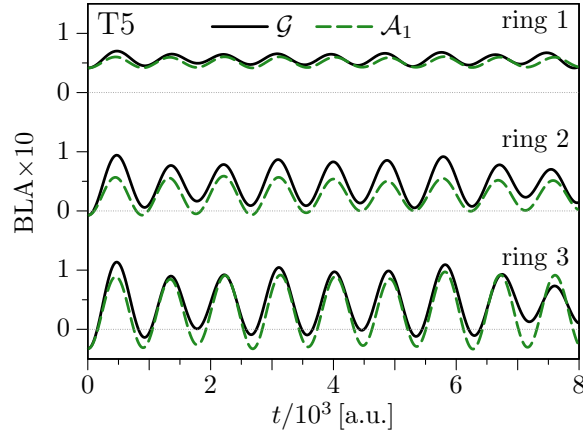


Figure 8. Time dependence of the bond length alternation (BLA) parameter during the dynamics induced by the emission in pentathiophene T5 [see Eq. (30) and Fig. 7]. The character of the outer rings (rings 1 and 2) is mainly aromatic (positive BLA), while the transition to the quinoid structure (negative BLA) occurs almost exclusively within the inner ring (ring 3).

require an a priori knowledge of the potential energy surfaces and the TGA approach remains robust for floppy molecules. No symmetry considerations are necessary; in particular, neither the dynamics nor the analysis relies on any symmetry assumptions. Moreover, further considerable gain in efficiency without loosing any substantial information can be obtained by employing Hessian interpolation.

Experimentalists try, often successfully, to translate the spectral features into a dynamical picture, which for theoreticians is often the starting point. The extraction of the essential information from the dynamical simulation, however, is often as difficult as the simulation itself. We presented, therefore, a novel systematic approach to identify groups of vibrations that are essential for the dynamics and for the spectrum. This approach even allowed us to compare different oligothiophenes T_n and to study changes in their spectra with increasing n : Their vibrational line shapes are modulated by inter-ring stretch and ring-squeeze vibrations, the latter contributing to the spectral broadening for longer chains. The ground and excited potential energy surfaces become more similar as the chain length increases; this, in turn, reduces the amplitude of the dynamics induced by emission and results in a shift of the intensity toward the 0–0 transition. The phenomenon is also reflected in the different dependences of the 0–0 and vertical transition energies on $1/n$.

The OTF-AI-TGA scheme also allowed us, by evaluating the bond length alternation,

Table I. Normal-mode classification based on decompositions (27) and (29) with $\varepsilon_B = 0.55$ and $\varepsilon_\rho = 0.6$ for the oligothiophene Tn family, $n \in \{2, 3, 4, 5\}$. Vibrational frequencies ω_i are given in cm^{-1} , while the maximum relative displacements ρ_i of Eq. (24) are dimensionless. The modes are further classified into 7 groups by the character of the deformation which they exert on the oligothiophene skeleton. These groups are distinguished by superscript labels next to frequency values. For schematic depiction of these deformations see Fig. 5.

class	group	$\omega_i [\text{cm}^{-1}]$				ρ_i			
		T2	T3	T4	T5	T2	T3	T4	T5
\mathcal{C}_1	\mathcal{A}_1	1657.7 ^(a)	1630.5 ^(a)	1615.5 ^(a)	1598.6 ^(a)	2.57 ^(a)	2.50 ^(a)	2.41 ^(a)	1.93 ^(a)
		1507.2 ^(a)	1553.9 ^(a)	1545.2 ^(a)	1590.1 ^(a)	1.23 ^(a)	1.10 ^(a)	1.12 ^(a)	1.35 ^(a)
		1450.0 ^(a)	1501.2 ^(a)	1581.3 ^(a)	1548.5 ^(a)	0.88 ^(a)	0.86 ^(a)	0.56 ^(a)	1.13 ^(a)
		1211.2 ^(a)	1461.9 ^(a)	1498.2 ^(a)		0.59 ^(a)	0.36 ^(a)	0.55 ^(a)	
		3243.6 ^(a)	1341.6 ^(a)	1462.6 ^(a)		0.25 ^(a)	0.34 ^(a)	0.36 ^(a)	
\mathcal{C}_2	\mathcal{A}_2	673.7 ^(b)	696.7 ^(b)	704.7 ^(b)	710.8 ^(b)	2.05 ^(b)	1.56 ^(b)	1.32 ^(b)	1.17 ^(b)
\mathcal{C}_3	\mathcal{A}_3	290.4 ^(e)	210.1 ^(e)	162.3 ^(e)	122.5 ^(c)	1.27 ^(e)	1.92 ^(e)	2.15 ^(e)	0.99 ^(c)
	\mathcal{A}_4	386.5 ^(c)	350.3 ^(c)	333.0 ^(c)	136.7 ^(c)	1.61 ^(c)	1.49 ^(c)	1.39 ^(c)	2.09 ^(c)
	\mathcal{A}_5	712.7 ^(g)	739.6 ^(g)	1112.9 ^(f)	322.6 ^(c)	1.09 ^(g)	0.64 ^(g)	0.63 ^(f)	1.35 ^(c)
	\mathcal{A}_6	1096.3 ^(f)	1261.6 ^(d)	1275.0 ^(d)	1109.5 ^(f)	0.78 ^(f)	0.70 ^(d)	0.66 ^(d)	0.78 ^(f)

to study directly dynamical oscillations between the quinoid and aromatic characters of individual rings in the oligothiophene chain.

OTF-AI-TGA is also useful as a preliminary test. The expensive OTF-AI information stored during the TGA simulation can be reused in other semiclassical methods such as poor person's Herman-Kluk (HK) propagator, where the HK prefactor is for all contributing trajectories assumed to be equal to the prefactor of the central trajectory.⁴⁸ In systems, which are too large to be treated with a more sophisticated quantum or semiclassical method, but for which the TGA is insufficient, e.g., due to the importance of interference effects, the analysis of the OTF-AI-TGA results can be used to define a subspace of reduced dimensionality, in which the most important dynamics occurs. Within this subspace, the effects that cannot be described with the TGA may be studied with less efficient yet better-suited

methods.²⁰ Alternative approaches for constructing the information-flow matrix in order to maximize the decoupling of the DOFs with minimal impact on the resulting spectrum are the subject of our ongoing research.

Finally, let us note that the computational protocol presented here is not limited to linear spectroscopy; non-linear spectra such as time-resolved stimulated emission can also be evaluated with the OTF-AI-TGA.

ACKNOWLEDGMENTS

This research was supported by the Swiss National Science Foundation with Grants No. 200020_150098 and National Center of Competence in Research (NCCR) Molecular Ultrafast Science & Technology (MUST), and by the EPFL.

Appendix A: TGA in subspaces of reduced dimensionality

One of the main goals of the normal mode analysis elaborated in Subsec. II E is identifying the normal modes essential for the dynamics. Restriction to these most important modes allows one to devise a simplified model of reduced dimensionality, e.g., in the spirit of the well-studied pyrazine vibronic coupling model.⁴⁹ Moreover, this reduction also broadens the class of computationally available methods. After the reduction, one may be able to employ, e.g., the Gaussian basis methods,⁵⁰ or various approaches from the family of the semiclassical initial value representation.⁵¹

Let us consider a system with D vibrational DOFs. In a typical OTF-AI-TGA calculation, one evolves the D -dimensional GWP by classically propagating its center x^t and by evaluating the phase factor γ^t and the complex time-dependent width matrix A^t by means of Lee and Heller's P - Z algorithm¹⁹ summarized in Subsec. II B [Eqs. (11) and (8)].

As in Subsec. II E, we identify the D -dimensional space of vibrational DOFs with the set $\mathcal{D} = \{1, \dots, D\}$. We would like to take advantage of the stored D -dimensional trajectory information, and, at the same time, to restrict ourselves to a subset $\mathcal{P} \subseteq \mathcal{D}$ of only $d < D$ most important vibrational degrees of freedom and define a linear projection $\pi: \mathbb{R}^D \rightarrow \mathbb{R}^d$ from the full space of D vibrational DOFs to the subspace of physical interest. Formally

$$\pi_{ij} := \delta_{\mathcal{P}_i, j} \text{ for } 1 \leq i \leq d \text{ and } 1 \leq j \leq D, \quad (\text{A1})$$

where \mathcal{P}_i denotes the i th element of the ordered set \mathcal{P} .

The “reduced” d -dimensional GWP is again propagated using the P - Z formalism. However, if (q^t, p^t) denotes the trajectory followed by the original, D -dimensional GWP, then the center of the reduced Gaussian follows a classical trajectory $(\pi \cdot q^t, \pi \cdot p^t)$ in the reduced, $2d$ -dimensional phase space. Also, the initial conditions for the time-dependent P^t , Z^t matrices must be replaced with

$$\bar{Z}^0 = \pi \cdot \pi^\top = I_d, \quad (\text{A2a})$$

$$\bar{P}^0 = 2i\hbar \pi \cdot A^0 \cdot \pi^\top. \quad (\text{A2b})$$

Here, d -dimensional matrices are denoted with a bar and A^0 is the initial width matrix of the D -dimensional GWP.

Finally, we need to isolate the \mathcal{P} -contribution to the effective Lagrangian \mathcal{L}_{eff} , which is required in Eq. (11) for evaluating the time-dependent complex phase γ^t . This is conveniently done using conservation of energy, since in all our calculations we consider only stationary initial states. Therefore

$$\frac{1}{2} \zeta^{t\top} \cdot \zeta^t + V(\eta^t) = V(\eta^0), \quad (\text{A3})$$

with ζ denoting momentum conjugated to η ; mass factors do not explicitly appear since η is already mass-scaled. Using Eq. (A3), the \mathcal{L}_{eff} -contribution to γ^t in Eq. (11) then reads

$$\begin{aligned} \int_0^t \mathcal{L}_{\text{eff}}^\tau d\tau &= \int_0^t \left[\frac{1}{2} (\zeta^\tau)^\top \cdot \zeta^\tau - V(\eta^\tau) \right] d\tau \\ &= \int_0^t \left[(\zeta^\tau)^\top \cdot \zeta^\tau - V(\eta^0) \right] d\tau \\ &= \int_0^t (\zeta^\tau)^\top \cdot \zeta^\tau d\tau - V(\eta^0) t. \end{aligned} \quad (\text{A4})$$

The part of this expression pertinent to the dynamics within the subset of vibrational DOFs \mathcal{P} is then easily obtained by replacing ζ^t with $\pi \cdot \zeta^t$, i.e.,

$$\int_0^t \mathcal{L}_{\text{eff}}^\tau d\tau \Big|_{\mathcal{P}} = \int_0^t (\pi \cdot \zeta^\tau)^\top \cdot (\pi \cdot \zeta^\tau) d\tau - V(\eta^0) t. \quad (\text{A5})$$

The term $V(\eta^0) t$ generates an overall phase depending linearly on t and is responsible only for shift of the resulting spectrum without altering its shape.

Appendix B: Analysis of the effective conjugation coordinate

Oligomer spectra are usually analyzed in terms of the so-called *effective conjugation coordinate*^{45–47} (ECC), i.e., the totally symmetric internal coordinate the excitation of which triggers the conformational change between the aromatic to the quinoid structures of the molecule. This approach is especially popular within Raman spectroscopy.^{43,52–55} For the oligothiophene family T_n , ECC captures the alternation between adjacent bonds and is defined as

$$\mathcal{R} := \frac{1}{\sqrt{\bar{N}}} \sum_{a=1}^{\bar{N}} (-1)^{a-1} r_a, \quad (\text{B1})$$

where r_a is the Cartesian vector connecting the a th and $(a+1)$ th carbon atoms of the backbone comprised of $\bar{N} = 4n - 1$ C-C bonds in total. Further insight is gained by restating Eq. (B1) in the normal-mode coordinates. By employing transformation (12), we obtain

$$\mathcal{R} = \mathcal{R}_{\text{ref}} + \mathbf{R} \cdot \boldsymbol{\eta}, \text{ with } \mathbf{R} := \mathbf{S} \cdot \mathbf{T} \text{ and } \mathcal{R}_{\text{ref}} := \mathbf{S} \cdot \boldsymbol{\xi}_{\text{ref}}, \quad (\text{B2})$$

where \mathbf{T} is the transformation matrix of Eq. (12), $\boldsymbol{\xi}_{\text{ref}}$ denotes Cartesian coordinates of a reference geometry, and

$$\mathbf{S} := \frac{1}{\sqrt{\bar{N}}} \sum_{a=1}^{\bar{N}} (-1)^a (\mathbf{P}_a - \mathbf{P}_{a+1}) \quad (\text{B3})$$

is a generalization of the projector \mathbf{P}_b defined below Eq. (13).

Then, the normalized “coupling strength” ν^j of the j th normal mode to \mathcal{R} reads

$$\nu^j := \frac{\text{Tr } \mathbf{Y}_j^T \cdot \mathbf{R}^T \cdot \mathbf{R} \cdot \mathbf{Y}_j}{\text{Tr } \mathbf{R}^T \cdot \mathbf{R}}, \quad (\text{B4})$$

where the square matrix \mathbf{Y}_j is defined as $(\mathbf{Y}_j)_{kl} := \delta_{jk}\delta_{jl}$.

However, the quantity \mathcal{R} changes during the dynamics and its variations are described in terms of

$$\delta\mathcal{R}^t := \mathcal{R}^t - \mathcal{R}^0 = \mathbf{R} \cdot \bar{\boldsymbol{\eta}}^t, \text{ with } \bar{\boldsymbol{\eta}}^t := (\boldsymbol{\eta}^t - \boldsymbol{\eta}^0). \quad (\text{B5})$$

Now, in order to asses the importance of a particular normal mode with respect to $\delta\mathcal{R}^t$, we can not use Eq. (B4) directly, since ν^j provides only a static picture. To remedy this, we introduce a more appropriate measure of dynamical coupling:

$$v^j := \frac{\varsigma^j}{\sum_k \varsigma^k}, \text{ with } \varsigma^j := \int_0^t dt \bar{\boldsymbol{\eta}}^t \cdot \mathbf{Y}_j^T \cdot \mathbf{R}^T \cdot \mathbf{R} \cdot \mathbf{Y}_j \cdot \bar{\boldsymbol{\eta}}^t, \quad (\text{B6})$$

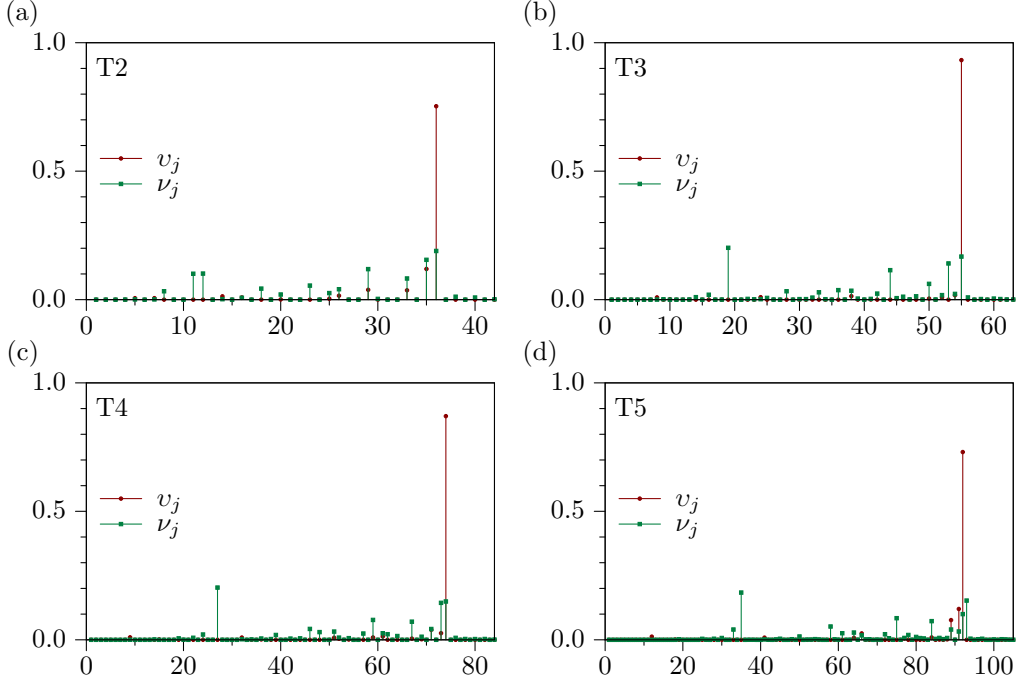


Figure 9. Comparison of the static, ν_j [see Eq. (B4)], and dynamic, v_j [see Eq. (B6)], contribution of individual normal modes to the ECC Υ of Eq. (B1) for the oligothiophenes T_n , $n \in \{2, 3, 4, 5\}$.

where the summation runs over all normal modes.

A comparison of individual normal modes for T_n , $n \in \{2, 3, 4, 5\}$, in terms of ν^j and v^j is shown in Fig. 9, which demonstrates clearly that only certain modes contributing to Υ are excited during the fluorescence process. This means that an analysis based merely on ν^j would be incomplete.

In Subsec. II E, individual normal modes were classified into independent groups \mathcal{A}_i [see Eq. (27)]. Using Eq. (B6), we can estimate the dynamical influence of a particular group \mathcal{A}_i on $\delta\Upsilon^t$ by employing

$$\kappa_i := \sum_{j \in \mathcal{A}_i} v^j. \quad (\text{B7})$$

Table II demonstrates that variations in Υ can be assigned mostly to the group \mathcal{A}_1 , and, hence, the α -peaks (see Fig. 3) originate from the change of the ECC during the dynamics induced by the fluorescence process.

	\mathcal{A}_1	\mathcal{A}_2	\mathcal{A}_3	\mathcal{A}_4	\mathcal{A}_5	\mathcal{A}_6
T2	0.947	0.013	0.006	0.006	0.008	0.015
T3	0.962	0.010	0.009	0.001	0.000	0.003
T4	0.942	0.009	0.010	0.002	0.004	0.013
T5	0.927	0.008	0.000	0.012	0.001	0.025

Table II. Contribution of the i th group \mathcal{A}_i to ECC in terms of κ_i introduced in Eq. (B7).

REFERENCES

- ¹I. F. Perepichka and D. F. Perepichka, eds., *Handbook of Thiophene-Based Materials* (John Wiley & Sons, Ltd, 2009); A. Mishra, C.-Q. Ma, and P. Bäuerle, Chem. Rev. **109**, 1141 (2009); I. F. Perepichka, D. F. Perepichka, H. Meng, and F. Wudl, Adv. Mat. **17**, 2281 (2005); H. Klauk, ed., *Organic Electronics: Materials, Manufacturing, and Applications* (Wiley-VCH Verlag, 2006).
- ²R. S. Becker, J. Seixas de Melo, A. L. Maçanita, and F. Elisei, J. Phys. Chem. **100**, 18683 (1996).
- ³A. Yang, S. Hughes, M. Kuroda, Y. Shiraishi, and T. Kobayashi, Chem. Phys. Lett. **280**, 475 (1997).
- ⁴A. Yang, M. Kuroda, Y. Shiraishi, and T. Kobayashi, J. Phys. Chem. B **102**, 3706 (1998).
- ⁵B. Thémans, W. R. Salaneck, and J. L. Brédas, Synthetic Metals **28**, 359 (1989).
- ⁶G. R. Hutchison, Y.-J. Zhao, B. Delley, A. J. Freeman, M. A. Ratner, and T. J. Marks, Phys. Rev. B **68**, 035204 (2003); S. S. Zade and M. Bendikov, Org. Lett. **8**, 5243 (2006).
- ⁷D. Jacquemin, A. Planchat, C. Adamo, and B. Mennucci, J. Chem. Theory Comput. **8**, 2359 (2012).
- ⁸F. J. Avila Ferrer, J. Cerezo, E. Stendardo, R. Improta, and F. Santoro, J. Chem. Theory Comput. **9**, 2072 (2013).
- ⁹M. Biczysko, J. Bloino, F. Santoro, and V. Barone, “Time-independent approaches to simulate electronic spectra lineshapes: From small molecules to macrosystems,” in *Computational Strategies for Spectroscopy* (John Wiley & Sons, Inc., 2011) pp. 361–443.
- ¹⁰J. Tatchen and E. Pollak, J. Chem. Phys. **128**, 164303 (2008); F. J. Avila Ferrer and F. Santoro, Phys. Chem. Chem. Phys. **14**, 13549 (2012); J. Cerezo, J. Zúñiga, A. Requena,

- F. J. Ávila Ferrer, and F. Santoro, *J. Chem. Theory Comput.* **9**, 4947 (2013).
- ¹¹E. Stendardo, F. Avila Ferrer, F. Santoro, and R. Improta, *J. Chem. Theory Comput.* **8**, 4483 (2012).
- ¹²R. Ianconescu, J. Tatchen, and E. Pollak, *J. Chem. Phys.* **139**, 154311 (2013).
- ¹³J. Tatchen and E. Pollak, *J. Chem. Phys.* **130**, 041103 (2009).
- ¹⁴M. Ceotto, S. Atahan, S. Shim, G. F. Tantardini, and A. Aspuru-Guzik, *Phys. Chem. Chem. Phys.* **11**, 3861 (2009); M. Ceotto, S. Atahan, G. F. Tantardini, and A. Aspuru-Guzik, *J. Chem. Phys.* **130**, 234113 (2009); M. Ceotto, S. Valleau, G. F. Tantardini, and A. Aspuru-Guzik, *ibid.* **134**, 234103 (2011); M. Ceotto, G. F. Tantardini, and A. Aspuru-Guzik, *ibid.* **135**, 214108 (2011).
- ¹⁵S. Y. Y. Wong, D. M. Benoit, M. Lewerenz, A. Brown, and P.-N. Roy, *J. Chem. Phys.* **134**, 094110 (2011).
- ¹⁶E. J. Heller, *J. Chem. Phys.* **62**, 1544 (1975).
- ¹⁷E. J. Heller, *Acc. Chem. Res.* **14**, 368 (1981).
- ¹⁸A. Lami and F. Santoro, “Time-dependent approaches to calculation of steady-state vibronic spectra: From fully quantum to classical approaches,” in *Computational Strategies for Spectroscopy* (John Wiley & Sons, Inc., 2011) pp. 475–516.
- ¹⁹S.-Y. Lee and E. J. Heller, *J. Chem. Phys.* **76**, 3035 (1982).
- ²⁰F. Grossmann, *J. Chem. Phys.* **125**, 014111 (2006).
- ²¹M. Baranger, M. A. M. de Aguiar, F. Keck, H. J. Korsch, and B. Schellhaaß, *J. Phys. A* **34**, 7227 (2001).
- ²²M. L. Brewer, J. S. Hulme, and D. E. Manolopoulos, *J. Chem. Phys.* **106**, 4832 (1997).
- ²³J. T. Hougen and J. K. G. Watson, *Canad. J. Phys.* **43**, 298 (1965).
- ²⁴I. Özkan, *J. Mol. Spec.* **139**, 147 (1990).
- ²⁵K. N. Kudin and A. Y. Dymarsky, *J. Chem. Phys.* **122**, 224105 (2005).
- ²⁶S. K. Kearsley, *Acta Crystallogr., Sect. A: Found. Crystallogr.* **45**, 208 (1989); E. A. Coutsias, C. Seok, and K. A. Dill, *J. Comp. Chem.* **25**, 1849 (2004).
- ²⁷V. Bakken, J. M. Millam, and H. Bernhard Schlegel, *J. Chem. Phys.* **111**, 8773 (1999); H. P. Hratchian and H. B. Schlegel, *J. Chem. Theory Comput.* **1**, 61 (2005).
- ²⁸J. M. Millam, V. Bakken, W. Chen, W. L. Hase, and H. B. Schlegel, *J. Chem. Phys.* **111**, 3800 (1999); U. Louderaj, K. Song, T. L. Windus, Y. Zhuang, and W. L. Hase, *ibid.* **126**, 044105 (2007); H. Wu, M. Rahman, J. Wang, U. Louderaj, W. L. Hase, and Y. Zhuang,

ibid. **133**, 074101 (2010).

²⁹M. Ceotto, Y. Zhuang, and W. L. Hase, J. Chem. Phys. **138**, 054116 (2013).

³⁰Y. Zhuang, M. R. Siebert, W. L. Hase, K. G. Kay, and M. Ceotto, J. Chem. Theory Comput. **9**, 54 (2013).

³¹G. H. Golub and C. F. van Loan, *Matrix Computations*, 3rd ed. (The Johns Hopkins University Press, 1996).

³²See Supplementary Material Document No. for details about the Hessian interpolation scheme, emission spectra of T3 and T4, time dependence of bond length alternation, first excited state equilibrium geometries, behavior of the OTF-AI-TGA GWP on PESs with indefinite Hessian, and comparison of the OTF-AI-TGA approach to the global harmonic approximation. For information on Supplementary Material, see <http://www.aip.org/pubservs/epaps.html>.

³³A. Peres, Phys. Rev. A **30**, 1610 (1984).

³⁴L. S. Cederbaum, E. Gindensperger, and I. Burghardt, Phys. Rev. Lett. **94**, 113003 (2005); D. Picconi, F. J. Avila Ferrer, R. Imrota, A. Lami, and F. Santoro, Faraday Discuss. **163**, 223 (2013).

³⁵G. Chartrand and P. Zhang, *A First Course in Graph Theory* (Dover Publications, 2012).

³⁶M. J. Frisch, G. W. Trucks, H. B. Schlegel, G. E. Scuseria, M. A. Robb, J. R. Cheeseman, G. Scalmani, V. Barone, B. Mennucci, G. A. Petersson, H. Nakatsuji, M. Caricato, X. Li, H. P. Hratchian, A. F. Izmaylov, J. Bloino, G. Zheng, J. L. Sonnenberg, M. Hada, M. Ehara, K. Toyota, R. Fukuda, J. Hasegawa, M. Ishida, T. Nakajima, Y. Honda, O. Kitao, H. Nakai, T. Vreven, J. A. Montgomery, Jr., J. E. Peralta, F. Ogliaro, M. Bearpark, J. J. Heyd, E. Brothers, K. N. Kudin, V. N. Staroverov, R. Kobayashi, J. Normand, K. Raghavachari, A. Rendell, J. C. Burant, S. S. Iyengar, J. Tomasi, M. Cossi, N. Rega, J. M. Millam, M. Klene, J. E. Knox, J. B. Cross, V. Bakken, C. Adamo, J. Jaramillo, R. Gomperts, R. E. Stratmann, O. Yazyev, A. J. Austin, R. Cammi, C. Pomelli, J. W. Ochterski, R. L. Martin, K. Morokuma, V. G. Zakrzewski, G. A. Voth, P. Salvador, J. J. Dannenberg, S. Dapprich, A. D. Daniels, Ö. Farkas, J. B. Foresman, J. V. Ortiz, J. Cioslowski, and D. J. Fox, “Gaussian 09 Revision C.01,” Gaussian Inc. Wallingford CT 2009.

³⁷M. Belletete, M. Leclerc, and G. Durocher, J. Phys. Chem. **98**, 9450 (1994).

³⁸J. E. Chadwick and B. E. Kohler, J. Phys. Chem. **98**, 3631 (1994).

- ³⁹R. S. Becker, J. S. de Melo, A. L. Maçanita, and F. Elisei, Pure Appl. Chem. **67**, 9 (1995).
- ⁴⁰J. Gierschner, J. Cornil, and H.-J. Egelhaaf, Adv. Mater. **19**, 173 (2007).
- ⁴¹D. Lumpi, E. Horkel, F. Plasser, H. Lischka, and J. Fröhlich, Chem. Phys. Chem. **14**, 1016 (2013).
- ⁴²D. Beljonne, J. Cornil, R. H. Friend, R. A. J. Janssen, and J. L. Brédas, J. Am. Chem. Soc. **118**, 6453 (1996).
- ⁴³D. Fazzi, E. V. Canesi, F. Negri, C. Bertarelli, and C. Castiglioni, Chem. Phys. Chem. **11**, 3685 (2010).
- ⁴⁴R. Ponce Ortiz, J. Casado, S. Rodríguez González, V. Hernández, J. T. López Navarrete, P. M. Viruela, E. Ortí, K. Takimiya, and T. Otsubo, Chem. Eur. J. **16**, 470 (2010).
- ⁴⁵G. Zerbi, C. Castiglioni, J. T. López Navarrete, T. Bogang, and M. Gussoni, Synthetic Metals **28**, D359 (1989).
- ⁴⁶J. Geisselbrecht, J. Kürti, and H. Kuzmany, Synthetic Metals **57**, 4266 (1993).
- ⁴⁷G. Zerbi, C. Castiglioni, and M. Del Zoppo, “Structure and optical properties of conjugated oligomers from their vibrational spectra,” in *Electronic Materials: The Oligomer Approach*, edited by K. Müllen and G. Wegner (Wiley-VCH Verlag GmbH, 2007) Chap. 6, pp. 345–402.
- ⁴⁸J. Tatchen, E. Pollak, G. Tao, and W. H. Miller, J. Chem. Phys. **134**, 134104 (2011).
- ⁴⁹G. Stock, C. Woywod, W. Domcke, T. Swinney, and B. S. Hudson, J. Chem. Phys. **103**, 6851 (1995).
- ⁵⁰D. V. Shalashilin and M. S. Child, J. Chem. Phys. **113**, 10028 (2000); G. A. Worth, M. A. Robb, and I. Burghardt, Faraday Discuss. **127**, 307 (2004); M. Ben-Nun and T. J. Martínez, Adv. Chem. Phys. **121**, 439 (2002).
- ⁵¹W. H. Miller, J. Phys. Chem. A **105**, 2942 (2001); M. F. Herman, Annu. Rev. Phys. Chem. **45**, 83 (1994); M. Thoss and H. Wang, *ibid.* **55**, 299 (2004); K. G. Kay, *ibid.* **56**, 255 (2005).
- ⁵²J. T. Lopez Navarrete and G. Zerbi, J. Chem. Phys. **94**, 965 (1991).
- ⁵³G. Zerbi, B. Chierichetti, and O. Ingäas, J. Chem. Phys. **94**, 4637 (1991).
- ⁵⁴C. Castiglioni, M. Tommasini, and G. Zerbi, Phil. Trans. R. Soc. Lond. A **362**, 2425 (2004).
- ⁵⁵E. Ortí, P. M. Viruela, R. Viruela, F. Effenberger, V. Hernández, and J. T. López Navarrete, J. Phys. Chem. A **109**, 8724 (2005).